RESEARCH ARTICLE

pss rrl
physica status solidi
www.pss-rapid.com

Modeling Photodetection at the Graphene/Ag₂S Interface

Davide Spirito,* Beatriz Martín-García, Vaidotas Mišeikis, Camilla Coletti, Francesco Bonaccorso, and Roman Krahne

Mixed-dimensional systems host interesting phenomena that involve electron and ion transport along or across the interface, with promising applications in optoelectronic and electrochemical devices. Herein, a heterosystem consisting of a graphene monolayer with a colloidal Ag₂S nanocrystal film atop, in which both ions and electrons are involved in photoelectrical effects, is studied. An investigation of the transport at the interface in different configurations by using a phototransistor configuration with graphene as a charge-transport layer and semiconductor nanocrystals as a light-sensitive layer is performed. The key feature of charge transfer is investigated as a function of gate voltage, frequency, and incident light power. A simple analytical model of the photoresponse is developed, to gain information on the device operation, revealing that the nanocrystals transfer electrons to graphene in the dark, but the opposite process occurs upon illumination. A frequency-dependence analysis suggests a fractal interface between the two materials. This interface can be modified using solid-state electrochemical reactions, leading to the formation of metallic Ag particles, which affect the graphene properties by additional doping, while keeping the photoresponse. Overall, these results provide analytical tools and guidelines for the evaluation of coupled electron/ion transport in hybrid systems.

1. Introduction

The synergic combination of nanomaterials with different dimensionalities, such as 2D materials and nanocrystals (NCs), is a promising strategy for application in optoelectronics, such as photodetectors,[1–8] as well as electrochemical devices[9] including memories[10–13] and sensing,[14,15] leveraging on the different characteristics of their components. The sensitivity of these hybrid systems to both their interface chemistry and physics and external stimuli such as light or electric field allows, on one hand, to develop efficient devices, and on the other hand, to study in depth the interface phenomena related to electron and ion transport.

For example, the optical absorption of NCs[5,16–18] can be combined with the excellent electrical conduction of graphene[19,20] in highly responsive hybrid NC/graphene phototransistors.[6,21–23] In these devices, photoexcitation occurs in the NC layer, and the physical separation of electrons and holes (which are transported to the graphene channel) induces a shift of the gate response of the graphene transistor resulting in a large light-induced current modulation. In this configuration, low light absorption in graphene and low electronic mobility in NC films are circumvented.[24] A similar approach can be extended also to other 2D materials.[25,26] The response efficiency and the speed of the device are related to the charge dynamics between the NC and the graphene layer,[8] and several interesting fundamental aspects can be investigated, such as the

Dr. D. Spirito
Materials Research
IHP–Leibniz-Institut für Innovative Mikroelektronik
Im Technologiepark 25, 15236 Frankfurt (Oder), Germany
E-mail: spirito@ihp-microelectronics.com

Dr. D. Spirito
Nanochemistry Department
Istituto Italiano di Tecnologia
Via Morego 30, 16163 Genova, Italy

Dr. B. Martín-García,[+] Dr. F. Bonaccorso
Graphene Labs
Istituto Italiano di Tecnologia
via Morego 30, 16163 Genova, Italy

Dr. V. Mišeikis, Dr. C. Coletti
Center for Nanotechnology Innovation @NEST
Istituto Italiano di Tecnologia
Piazza San Silvestro 12, I-56127 Pisa, Italy

Dr. F. Bonaccorso
BeDimensional S.p.A.
Via Lungotorrente Secca 3d, 16163 Genova, Italy

Dr. R. Krahne
Optoelectronics
Istituto Italiano di Tecnologia
Via Morego 30, 16163 Genova, Italy

effect of light power, or the frequency response of the device, toward improved performances compared to reported figures of merit.[2]

For other applications, such as memory devices[27–29] or neuromorphic computation,[30–32] it is important to assess the role of ion transport and electrochemical reactions at the interface.

In these cases, graphene, for its inert nature, can serve as a counter electrode[33,34] in devices in combination with mixed ion–electron conductors, and allow for good electronic conduction that enables solid-state reactions.[35] Good ion conduction can result from a crystal structure in which activation energy for favorable interstitial location of mobile ions is low,[36] or, in the case of NCs and nanostructured materials, from the presence of defects and grain boundaries.[35,37]

In addition to the research efforts focused on device performance, one of the key tools toward the development of efficient devices is the understanding of the interface properties.[2,8,38,39] To this aim, several techniques, such as time-resolved optical spectroscopy[40–42] and scanning probe microscopy,[43,44] have been applied, but they require specialized equipment and careful protocols. Photocurrent response measurements, on the other hand, are commonly used in device characterization for the estimation of the figures of merit; in addition, they can provide valuable information on the phenomena involving light absorption and charge dynamics at the interface, when supported by a device model that can be easily implemented and extended.[45]

Therefore, here, we study a multifunctional device for interface modeling purposes, comprising a Ag_2S NC layer crossbar atop a graphene monolayer. Ag_2S NCs have demonstrated promising perspective as nontoxic material for photodetectors.[4,46] The Ag_2S NCs can serve several purposes as follows: 1) it is a semiconductor which can act as a light absorber, 2) it is a ionic conductor, and 3) it can host solid-state reactions (with the help of an active Ag electrode) to have the in situ formation of metallic Ag particles.[47] In fact, because of properties (2) and (3), Ag_2S has been successfully used for memories.[27,47–50] We use graphene as a back-gated

field-effect transistor (FET), thus enabling phototransistor measurements. The proposed design has, in principle, several operation modes: phototransistor, photodiode, memristor, or optical memory,[10] of which we describe potentiality and limits. At the same time, it enables an in-depth study of interface effects on ionic and electronic transport. Concretely, we focus on the photodetection experiments using the photoinduced doping due to charge transfer between NCs and graphene, which provide interesting information on the nature of the interface. We developed a simple analytical model to describe the device behavior. In addition, using solid-state reaction in the NC layer, we show the effect of the formation of metallic Ag particles on the device, and visualize the ion transport paths in the Ag_2S NC layer.

The developed model allows to identify, in the photoresponse, the contribution of the different components of the device, and to find the type of doping and photodoping, and the frequency response of the phototransistor, contributing to a solid foundation for understanding of photodetectors built with graphene and NCs, as well as other hybrid devices.

2. Device Design and Fabrication

The device design is a crossbar geometry with a large graphene transistor overlapped by a patterned layer of colloidal Ag_2S NCs (**Figure 1**a,b), defined by electron beam lithography (EBL) (see the Experimental section for details). The graphene layer (grown by chemical vapor deposition, CVD, and transferred onto a Si/SiO_2 substrate) has Ti/Au ohmic contacts, whereas two different electrodes were made for the NCs layer: Ti and Ag, the latter to allow the electrochemical conversion of the Ag_2S NCs to metallic Ag particles, and therefore to manipulate the interface.

We first describe the characteristics of the graphene, then how the incorporation of the Ag_2S NC layer affects the electrical properties of the graphene transistor and phototransistor.
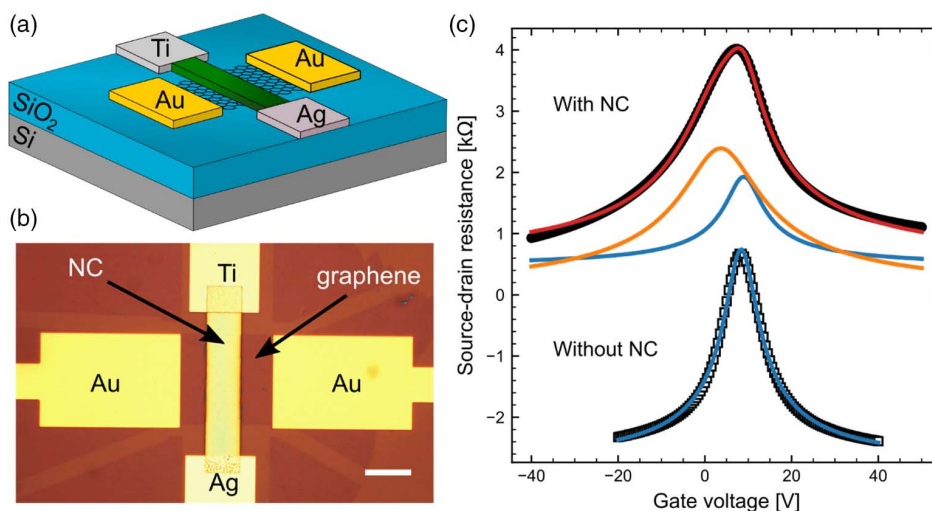

Figure 1. a) Scheme of the device design. b) Optical image of a standard devices. Scale bar is 20 µm. c) Source–drain resistance measured at a source–drain bias of 0.1 V, as a function of gate voltage for Device A, acquired in the dark before (lower part) and after (upper part) the NC deposition. Lower curve is offset by −3 kΩ for clarity. Symbols are experimental data. The orange and blue curve for the upper part are the two terms as described in Equation (2). The red curve is the complete fit.

Table 1. Best fit parameters for the data reported in Figure 1c. Length (L) and width (W) are fixed.

	V_{D1} [V]	n_{01} [10^{12} cm^{-2}]	μ_1 [cm^2 V^{-1} s^{-1}]	L_1, W_1 [µm]	V_{D2} [V]	n_{02} [10^{12} cm^{-2}]	μ_2 [cm^2 V^{-1} s^{-1}]	L_2, W_2 [µm]
Without NC	$+8.37 \pm 0.02$	0.280 ± 0.002	6230 ± 60	40, 40				
With NC	$+8.9 \pm 0.2$	0.31 ± 0.04	8500 ± 2500	25, 40	$+3.7 \pm 0.5$	0.65 ± 0.01	1500 ± 170	15, 40

Finally, by using a solid-state reaction to partially convert the Ag_2S NCs to Ag particles, we study the photoresponse of the resulting device.

The source–drain resistance versus gate voltage curve (R_{sd}–V_G) of the graphene FETs (GFETs) before Ag_2S NC layer deposition (Figure 1c, lower part) has a symmetric peak around the Dirac point at $V_G \approx +8$ V, indicating p-type doping. To analyze the electrical properties, we use a simple model for the GFET,[51] valid for small source–drain voltage. It includes the residual carrier density n_0 and a single field-effect mobility μ for electrons and holes

$$R(V_G, V_D) = \frac{1}{e \frac{W}{L} \mu \sqrt{n_0^2 + \frac{C_G^2}{e^2}(V_G - V_D)^2}} \quad (1)$$

where W and L are the width and length of the channel, and C_G the gate capacitance per unit area; a constant series resistance R_c can also be added. The experimental curve is well fitted by this model. The best fit for the bare graphene gives $n_0 \approx 0.3 \times 10^{12}$ cm^{-2} and $\mu \approx 6000$ cm^2 V^{-1} s^{-1}, as reported in **Table 1**.

The incorporation of the NC layer modifies the R_{sd}–V_G curve (Figure 1c, upper part). The curve has a broader peak, and it is slightly asymmetric. To address the modified device, we extend the model in Equation (1) considering the series of two GFETs, and we write the total resistance as the sum

$$R_{sd}(V_G) = R_C + R_1(V_G, V_{D1}) + R_2(V_G, V_{D2}) \quad (2)$$

The two terms can be assigned to the part not covered with NCs (bare graphene) and the part covered with NCs (graphene/NC heterostructure). The best fit yields a component (R_1) with Dirac voltage and residual carrier density corresponding to that observed for bare graphene (see Table 1), and therefore attributed to the noncovered part. The second component R_2 has Dirac voltage shifted toward $V_G = 0$ V and almost twice the residual carrier density, and is ascribed to the graphene/NC heterostructure part. The mobility of R_2 is much lower than R_1, related to scattering from NC/graphene interface.

This behavior is reproducible in other devices, whose R_{SD}-V_G curves after NCs deposition show a broad asymmetric peak, well reproduced by Equation (2). In all cases, the component assigned to the NC-covered part presents a Dirac voltage close to 0 V or even at negative voltage, indicating a n-doping due to charge transfer and the change in the dielectric environment of the graphene, both inducing a shift of the Fermi energy.[52–54]

3. Photocurrent Response

As the semiconductor Ag_2S NCs can act as light absorber, we evaluated the photoresponse of the crossbar device without further preparation in a phototransistor configuration, to verify the charge-transfer efficiency across the interface. We have

therefore used a blue laser (472 nm), thus with excitation well above the bandgap of the NCs,[47] to ensure full absorption of the light in the NC layer. Measurements were performed in vacuum.

The focused light was modulated by a chopper, and the current flowing in the GFET was measured using a current amplifier and lock-in amplifier, as a function of gate voltage. At the same time, also the DC current was measured. Further details are reported in the Experimental Section.

Figure 2 reports the photoresponse as a function of gate voltage: the DC resistance (measured as the ratio of DC current and applied source–drain bias) in dark and under light, the AC current magnitude, and the phase of the AC signal. In Figure 2a, the DC resistance under light is slightly shifted (≈ -1 V) toward negative gate voltage with respect to the curve in dark. These curves can be analyzed using Equation (2), finding two resistors in series with Dirac point at -1.2 V (R_1, blue curve) and -8.5 V (R_2, orange curve).

The AC photocurrent is therefore a small perturbation over the dark current. As shown in the Figure 2b, its magnitude is zero near -6 V, and has an inflection point around -1.2 V. We assign the zero of the AC photocurrent at -6 V to the photosensitive graphene/NC heterostructure, and its inflection at
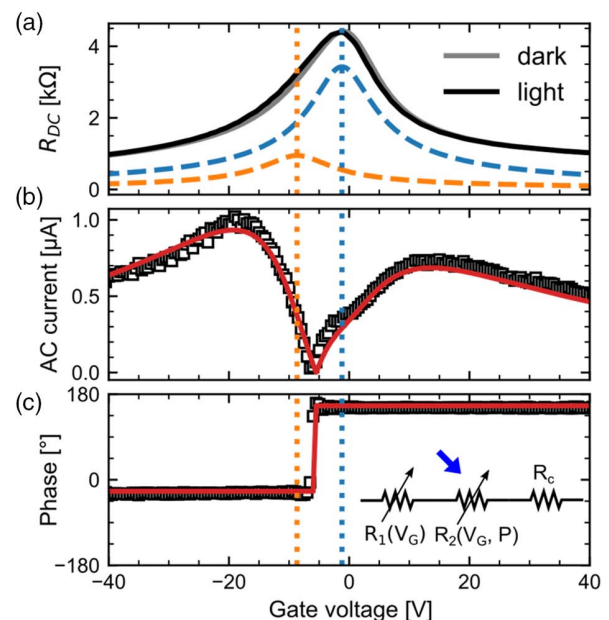
Figure 2. a) DC resistance as a function of gate voltage for Device B, measured in the dark and under light (1.9 µW on device). The dashed curves are the components extracted using Equation (2). Dotted lines mark the position of the Dirac point of these curves. b,c) Amplitude and phase of AC photocurrent. The red curve in (b) is a fit with Equation (4), and in (c), the phase calculated from combination of Equation (4) and (5). The inset in panel (c) illustrates the model described in the text.

ADVANCED SCIENCE NEWS
www.advancedsciencenews.com

pss
physica status solidi **rrl**
www.pss-rapid.com

−1.2 V, which corresponds to the R_1 Dirac point, to the bare graphene. Therefore, R_1 is acting as gate-dependent load to the R_2 phototransistor (see inset in Figure 2c).

In correspondence to the zero of the AC photocurrent, the phase of the AC signal changes by 180°, i.e., the photocurrent changes its polarity, as expected.[8] The exact determination of the phase (detailed in the Experimental Section) reveals that it is shifted by ≈−30° with respect to the values of 0° and 180°, which would be expected for a standard photoresistor-like device. In fact, the observed shift is an indication of complex charge transfer and trapping effects, as will be discussed in the following sections.

For a full assessment of these features, we derive a suitable formula for the response of the phototransistor. To this aim, the photocurrent can be calculated as the difference of current under light and dark. Using Equation (2), we consider R_2 as dependent on the light, resulting in a gate voltage shift ΔV_D that sums to V_{D2}. In this way, R_2 is a gate-dependent photoresistor (phototransistor), and R_1 is a gate-dependent load resistor. This results in the formula

$$I_{\text{photocurrent}} = V_{sd}\left(\frac{1}{R_C + R_1(V_G, V_{D1}) + R_2(V_G, V_{D2} + \Delta V_D)} - \frac{1}{R_C + R_1(V_G, V_{D1}) + R_2(V_G, V_{D2})}\right) \quad (3)$$

where V_{sd} is the source–drain bias.

From this equation, the zero of the photocurrent occurs at $V_G^{(0)}$ satisfying $R_2(V_G^{(0)}, V_{D2} + \Delta V_D) = R_2(V_G^{(0)}, V_{D2})$, which, using Equation (1), corresponds to $V_G^{(0)} = V_{D2} + \Delta V_D/2$. With $V_{D2} = -8.5$ V and $V_G^{(0)} = -6$ V from the data in Figure 2, we find a positive $\Delta V_D = +5$ V, indicating a p-type photoinduced doping of about 4×10^{11} cm^{-2}. The p-type doping is further confirmed by the polarity of the photocurrent. Indeed, leaving out for a first analysis the small phase shift, we can assign positive photocurrent for $V_G < V_G^{(0)}$ and negative photocurrent for $V_G > V_G^{(0)}$. These signs occurs if ΔV_D is positive, whereas a negative value for ΔV_D would lead to the opposite (negative photocurrent for $V_G < V_G^{(0)}$). In fact, the alternative interpretation of R_1 as light-dependent resistor, thus using $V_{D1} = -1.2$ V, would lead to a negative ΔV_D, which is incompatible with the experimental data. This further confirms our identification of the NC-covered and noncovered graphene parts.

To discuss in more detail the amplitude and phase dependence of the photocurrent on the gate voltage, we consider the light modulation as a small signal over the dark response of the device, as visible in Figure 2a. In particular, light is a small modulation of the Dirac voltage V_{D2}, so that the photocurrent can be written as

$$I_{AC} = \frac{\partial I}{\partial V_{D2}} \Delta V_D$$
$$= V_{sd} \frac{\partial}{\partial V_{D2}}\left(\frac{1}{R_C + R_1(V_G, V_{D1}) + R_2(V_G, V_{D2})}\right)\Delta V_D$$
$$= V_{sd}\left[-\frac{R_2(V_G, V_{D2})^3}{(R_C + R_1(V_G, V_{D1}) + R_2(V_G, V_{D2}))^2}\right] \quad (4)$$
$$\times \left(\frac{\mu C_G W}{L}\right)^2 (V_G - V_{D2})\Delta V_D$$

The modulated light power can be considered as a sum of DC component (the average power of the light) and a frequency-dependent expansion, of which we measure only the 1st harmonic with the lock-in amplifier (AC part). This AC amplitude is inserted in Equation (4) as ΔV_D, and can be in general written as a complex function of the frequency $\Delta V_D(\omega)$, to take into account the frequency of the modulation as well as the possible phase shift between the modulated light and the photocurrent. In this way, ΔV_D acts as an optoelectrical transfer function.[55]

The model in Equation (4) can therefore be readily compared with the data in Figure 2b. An excellent fit of the data can be obtained for the amplitude, as shown in the figure as red curve.

To explore the function $\Delta V_D(\omega)$, and shed light on the frequency shift observed in Figure 2c, we have studied the photocurrent amplitude at gate voltage −20 V (near the maximum value shown in Figure 2b) in the range 23–1000 Hz, as shown in **Figure 3**a,b (see Figure S1 and S2, Supporting Information, for additional data from a different device).

We find that the amplitude is decreasing for increasing frequency, approximately with a power law $f^{-1/3}$. For standard photoresistors, a low-pass behavior is expected, i.e., a constant amplitude followed by a $1/f$ decrease at high frequency. The observed trend can be instead described as a constant-phase element (CPE) response, i.e., the ΔV_D appearing in Equation (4) can be written as

$$\Delta V_D(\omega) = \frac{A}{(j\omega)^n} \quad (5)$$

From the data in Figure 3a, we calculate $n = 0.270 \pm 0.006$. The parameter A is related to the efficiency of the charge excitation and transport, and can be positive or negative according to the sign of the transferred charges; its sign will determine the polarity of the photocurrent. This equation predicts also a phase shift for the photocurrent of $-90° \cdot n \approx -30°$. This phase shift is well reproduced in the frequency dependent data of Figure 3a,b; furthermore, inserting Equation (5) in (4), we reproduce the phase dependence in Figure 2c. Consistently with the previous observation, the parameter A is found to be positive. This multiple validation of phase value and amplitude trend supports the CPE with $n \approx 1/3$ value.

Anomalous frequency dependence[56,57] or, correspondingly, time responses,[8,45] are often reported in nanostructured photodetectors, and ascribed to a continuous distribution of time scales in the system due to trap states. The physical origin of the CPE behavior in such systems, and in the NC/graphene heterostructure in particular, can be attributed to the diffusion of photoexcited charges in the disordered NC film and at its interface with graphene. In general, anomalous diffusion is associated with disordered systems and interfaces,[58–60] such as the case of porous electrodes. It has been shown that a description of the interface as a fractal leads to a frequency response of constant-phase type, with the coefficient n depending on the fractal dimension.[61,62] This mathematical framework provides an explanation to the "anomalous" time and frequency dependence observed in nanostructured photodetectors. Our results provide a strong support for their experimental evaluation due to the
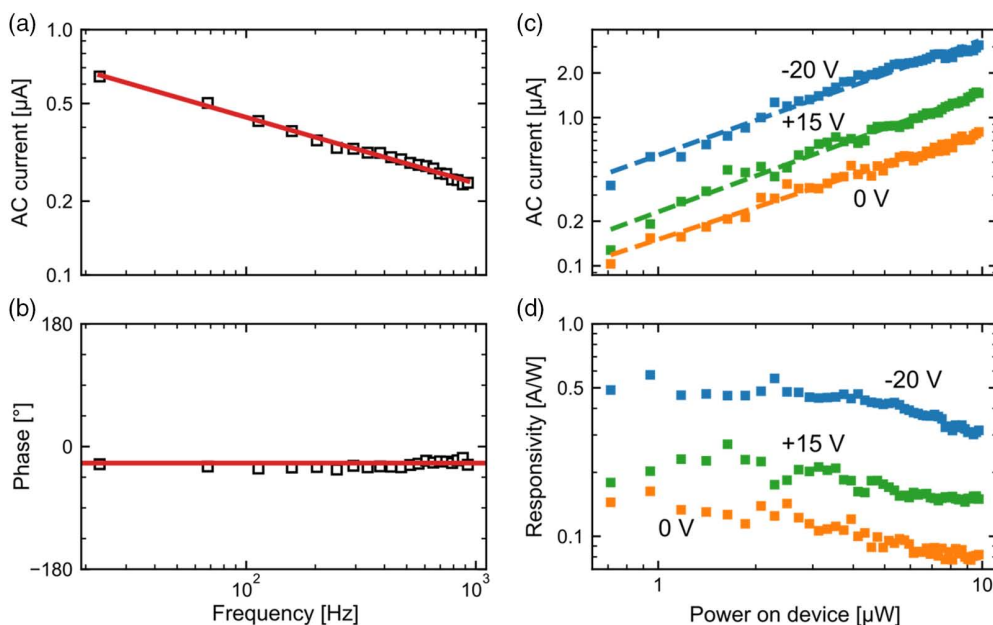
Figure 3. a,b) Frequency dependence of the AC photocurrent at $V_G = -20$ V and power = 1.9 μW for device B. The continuous red lines are CPE dependence (Equation (5)) with $n = 0.27$. c) Power dependence of the AC photocurrent at different gate voltage, at 23 Hz. Dashed lines are power-law fits. d) Power dependence of responsivity; "power on device" is the power of the light over the area of the NC-covered graphene.

modeling and the proper evaluation of the phase shift, and can give some additional insights. Indeed, we observe the same frequency trend independently from the gate voltage (see Figure S3, Supporting Information), suggesting that the graphene doping is not affecting the charge dynamics, differently from the studies by Tielrooij et al. and Prasai et al.[40,63] In a similar experiment with PbS NCs on graphene,[24] the standard low-pass response was observed, indicating smoother interface than in our case, and highlighting the key role of the interface for device speed.

To complete the characterization of the device, we have measured the power dependence of the photocurrent (Figure 3c) at gate voltage of −20, 0, and +15 V, corresponding to the maximum positive photocurrent, the maximum negative photocurrent, and a value close to the zero. We found that the photocurrent is slightly sublinear as a function of power, but with comparable trends for all the cases. A power-law fit (shown in the Figure 3c as dashed lines), yields exponents 0.78 ± 0.02, 0.72 ± 0.02, and 0.81 ± 0.02 for gate voltage of −20, 0, and +15 V, respectively. The resulting responsivity (the ratio of the photocurrent to the light power), shown in Figure 3d, decreases with the power, and reaches ≈0.5 A W^{-1} at the low power. The phase of the AC current is found to be independent on power (see Figure S3, Supporting Information). The sublinear power dependence is often observed in nanostructured photodetector, together with the anomalous frequency response,[64] and similarly, can be attributed to nonlinear dynamics of charge transfer and recombination.[56] It can as well be described as the interplay of shallow and deep defect levels,[65] or more in general as the effect of trap states on the relaxation of photoexcited charges.[66–68]

4. Formation of Ag Particles and Its Effect on the Photoresponse

The availability of Ag$_2$S NCs and active (Ag) contacts allows to perform electrochemical cycles on the device to modify the interface. Considering the device design and geometry, we can exploit not only Ti but also graphene as inert electrode. The result of the electrochemical cycles is the formation of micrometer-sized metallic Ag particles, which result from the Ag$^+$ reduction reaction occurring in the NC layer, together with the migration of Ag$^+$ from the Ag contact.[47] Particles formed on the device after voltage application between Ti and Ag electrodes are shown in **Figure 4**. These Ag particles are formed, namely, on the NC layer that is not overlapped with graphene. Some Ag particles appear also at the edges of the NC bar, where electrons from the graphene are available. This fact can be understood as an effect of the spatial separation between the Ag$^+$ ions, which move in the NC layer, and the electrons, which are flowing in the highly conductive graphene layer where the two layers overlap. Therefore, the reduction reaction occurs only when the two species are not physically separated. When using graphene as inert electrode, the metallic Ag particles formation happen in a less uniform way, leading to an unstable electrical response, but demonstrating the potential of graphene as inert electrode (See Figure S4, Supporting Information).

Because of this, we use the Ti–Ag electrodes only to generate the Ag particles, and indeed, the in situ formation of Ag particles is a demonstration of the occurrence of solid-state reactions in our device. Instead of electrochemical measurements applied to the measurement of ion conductivity in the NC layer, we rely on the graphene FET electrical and optoelectronic response, so that a study of their effect on photoresponse is possible.[69]
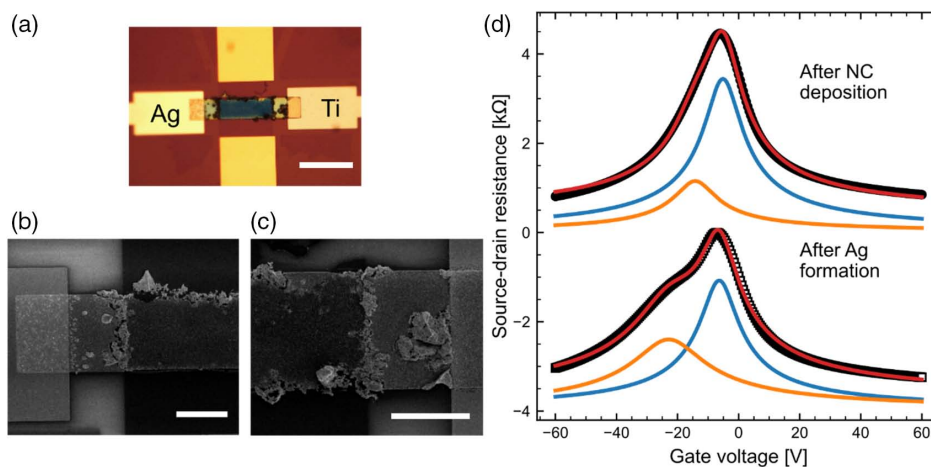
Figure 4. a) Optical microscopy image of Device C after formation of Ag particles following the application of electrochemical cycles. Scale bar is 40 µm. b,c) Scanning electron microscopy (SEM) images of the Ag and Ti electrodes, respectively. Scale bars are 10 µm. d) Source–drain resistance as a function of gate voltage for Device C, acquired in the dark after NC deposition and before (lower part) and after (upper part) the formation of the Ag particles. The lower curve is shifted by −4 kΩ for clarity. Symbols are experimental data. The orange and blue curves are the two terms as described in Equation (2). Red is the full fit curve.

The R_{sd}–V_G curve for the device is shown in Figure 4d, before and after the voltage application to the Ti–Ag electrodes inducing the formation of metallic Ag particles. After NC deposition, the device exhibits the two-resistor response (Equation (2)), with both covered and noncovered part having Dirac point at negative voltage (n-type doping). After the electrochemical cycle, the curve has a clear shoulder around −20 V. As shown in Figure 4d and in **Table 2**, the results of the fit with Equation (2) verify that the noncovered part is not modified by the metallic Ag particle formation, whereas the covered part is more n-doped (Dirac point from −14 to −23 V), and its mobility is less than half the initial value. This is reflected in the observed modification on the device (Figure 4a–c): 1) increase in the roughness of the interface and 2) partial change in the character of the particles from semiconductor to metallic.

The phototransistor measurements after the formation of metallic Ag particles are shown in **Figure 5**. The AC photocurrent trend has the same features of the previous case (without metallic Ag particles). Its amplitude has a zero around −30 V, and a local minimum around −10 V. The small-signal model in Equation (4) reproduces well the data (dotted line in Figure 5), revealing that the local minimum is related to the noncovered part of the graphene channel acting as a load.

When measuring with increasing light power (Figure 5a), we note that the AC photocurrent does not increase with the light power (Figure 5d). It first increases (passing from 0.1 to 1.2 µW), but for higher power decreases. Also, the zero of the AC current appears to be shifting toward $V_G = 0$ V as shown in Figure 5c, but it does not follow the increase in power.

Nonetheless, the photoinduced doping is verified to be positive: as observed in the case of Figure 3c, the phase change shown in Figure 5d can be explained only by a positive ΔV_D. Thus, despite the formation of metallic Ag particles, we still observe a p-type photoinduced doping of graphene. The unstable response that we observe can be due to a modification of the NC layer caused by photoinduced heating enhanced by metallic particles or light-induced reduction of Ag_2S NCs to metallic Ag.[70,71] Indeed, after the measurements with light, we observe a shifted R_{sd}-V_G characteristics in dark (see Figure S5, Supporting Information).

The responsivity for the device after Ag formation reaches 1.0 A W^{-1}, a small improvement over the 0.5 A W^{-1} for the Ag_2S device, which might be related to plasmonic enhancement.[69]

Focusing on the phase shift observed in Figure 5b,e, we note that with respect to the case of a device without metallic particles, the phase is not fixed at ≈−30°, but is different for different power, ranging from ≈−75° at low power to −34° at high power. This power-dependence shift reveals that a change in the interface may happen during the measurements, indicating that the analysis of the AC photoresponse together with the model gives insight in such a complex mixed heterostructure, and provides solid understanding on the doping and photoinduced charge transfer, as well as the dynamics of the transport phenomena occurring at the interface.

5. Conclusion

We have fabricated devices with a crossbar geometry comprising a CVD graphene monolayer and a film composed by Ag_2S NCs.

Table 2. Best fit parameters for the data reported in Figure 4d. Length (*L*) and width (*W*) are fixed.

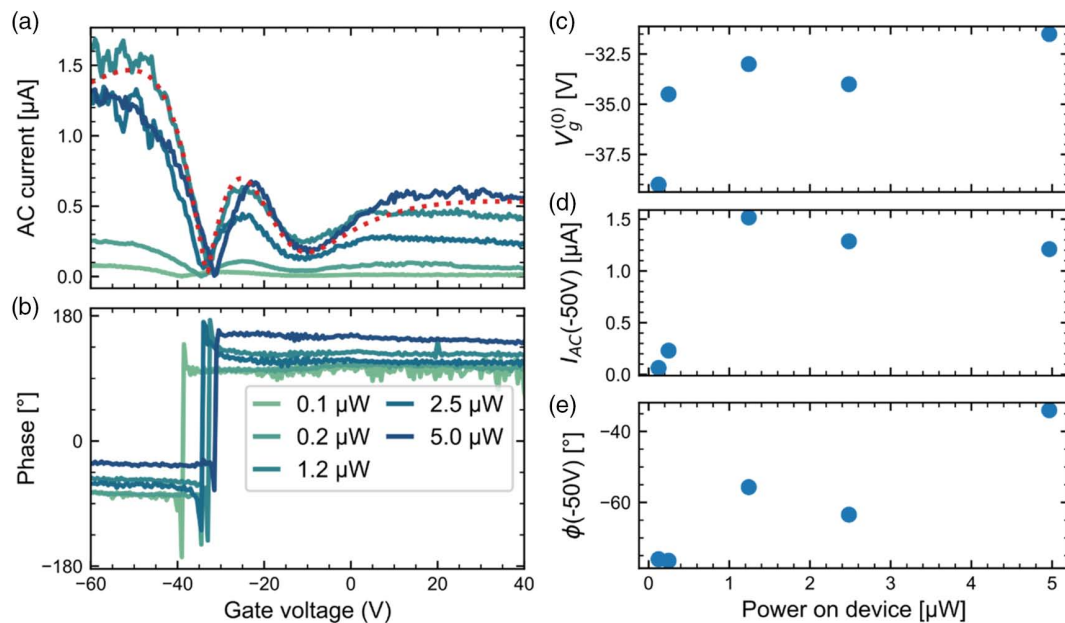|	V_{D1} [V]	n_{01} [10^{12} cm^{-2}]	μ_1 [cm^2 V^{-1} s^{-1}]	L_1, W_1 [µm]	V_{D2} [V]	n_{02} [10^{12} cm^{-2}]	μ_2 [cm^2 V^{-1} s^{-1}]	L_2, W_2 [µm]
After NC deposition	−5.1 ± 0.1	0.444 ± 0.009	2550 ± 120	25, 40	−14.2 ± 0.5	0.50 ± 0.03	4081 ± 540	15, 40
After Ag formation	−6.3 ± 0.1	0.447 ± 0.007	2981 ± 75	25, 40	−22.9 ± 0.3	0.84 ± 0.02	1741 ± 70	15, 40

Figure 5. a,b) Amplitude and phase of photocurrent acquired from Device D at different light power, at 23 Hz. The red, dotted curve in (a) is a fit with Equation (4) for data at 1.2 µW. c–e) Dependence on the light power of the zero of the AC photocurrent, the AC photocurrent magnitude, and phase at $V_G = -50\,V$.

In this heterostructure, the graphene acts as FET with the use of the doped substrate. The deposition of the NCs atop the device results in a transfer of electrons to the graphene in the region covered by the NCs. The two regions (NC-covered and noncovered) can be readily identified applying our analytical model to the measurement of the transistor current as a function of gate voltage. By illuminating the device with modulated light, a photoresponse is measured, which is determined by the p-type photodoping of graphene. The device is considered as a series of a phototransistor and a load transistor: the NC-covered and noncovered regions, respectively. In this way, we have developed a model that reproduces all the features of the gate-dependent photocurrent. The analysis of the phase and frequency dependence of the photoresponse shows a constant-phase-like response, which is attributed to the fractal nature of the interface between the two materials. This type of response to light modulation frequency in term of a "fractional capacitor" can find application for robust control, e.g., in robotics.[72]

Finally, applying a voltage across the NC bar yields the formation of metallic Ag particles through electrochemical solid-state reaction. These particles affect the graphene device by inducing further n-type doping. The main features of the response can be extracted from comparison with the model, indicating a photoinduced p-type doping and a modification of the interface compared to the case without metallic particles.

6. Experimental Section

Graphene Growth: Large-crystal graphene was grown in a cold-wall CVD reactor on 25 µm Cu foil (Alfa-Aesar) using CH_4 as the carbon source at a temperature of 1070 °C.[73] The graphene was then transferred to Si/SiO$_2$ substrates using semi dry–dry transfer.[74] Briefly, the graphene crystals

were coated with a poly(methyl methacrylate) (PMMA) membrane and a frame was attached to the perimeter of the sample. Graphene/PMMA was delaminated from Cu in 1 M NaOH solution and rinsed in water. The membrane (supported by the frame) was then laminated to the target substrate in air using a dedicated transfer setup.[75] Finally, the polymer was removed in acetone and isopropanol.

$Ag_{2-x}S$ Synthesis: The synthesis of colloidal metal Ag-doped $Ag_{2-x}S$ NCs was conducted following our published protocol.[47] Briefly, AgNO$_3$ (68 mg, 99.8%, Sigma Aldrich), oleylamine (1 mL, 80–90%, Across Organics), oleic acid (5 mL, 90%, Sigma Aldrich), and octadecene (10 mL, 90%, Sigma Aldrich) were mixed and degassed under vacuum in a Schlenk line at 95 °C for 2 h, obtaining a clear yellowish solution. The flask was then heated to 115 °C, and a solution of S-oleylamine (1 mL, 0.075 M) was quickly injected. The synthesis was quenched after 1 min by cooling to room temperature. The NC suspension was purified (in air) by using two washing steps with acetone and ethanol, and then, dried under a N_2 flow. Finally, the NCs were dispersed in toluene and filtered with a 0.2 µm poly(tetrafluoroethylene) filter membrane (Sartorius) to be used for device fabrication (30 mg mL^{-1}) by spin coating and solid ligand exchange procedures using tetramethylammonium iodide in MeOH in a glove box, as previously described in our works.[47,76,77]

Device Fabrication: GFETs and crossbar NC structures were pattered by EBL (Raith 150-Two), using PMMA as resist (≈160 nm thickness). Ohmic contacts to the graphene were made by Ti(5 nm)/Au(40 nm) deposited by e-beam evaporator (Kenosistec), at a deposition rate of 0.3 Å s^{-1} and a base pressure of about 10^{-6} mbar, followed by liftoff in acetone. Ar/O$_2$ plasma was used to etch the graphene layer and define the transistor channel. Spin coating of the Ag$_2$S NC solution onto the patterned PMMA, followed by liftoff, was used to define the NC bar. Contacts to the NC bar were deposited by e-beam deposition followed by liftoff, and consisted of Ti(40 nm)/Au (5 nm) and Ag(40 nm)/Au(5 nm). The graphene channel had both length and width of 40 µm, and the crossbar a length of 15 µm, extending across the whole graphene channel (Figure 1a,b).

Scanning electron microscopy (SEM) images were acquired using a Helios Nanolab 600 (FEI), at an accelerating voltage of 10–20 kV and a beam current of 0.2 nA. Optical microscope images were taken with a Nikon Eclipse LV100.

Photocurrent Measurement: For photoresponse measurements, the sample was mounted in a vacuum ($\approx 5 \times 10^{-5}$ mbar) probe station (Janis) with optical access. A fiber-coupled diode laser (472 nm) was used; the power was tuned via DC signal applied to the controller. The output of the fiber was focused on the sample by a lens, with a spot size of $\approx 400\,\mu m$. The power reaching the sample was measured by a calibrated power meter (Thorlabs S120VC). A mechanical chopper was used for light modulation.

Electrical setup for measurements consisted of a two-channel Keithley K2600 Source-meter unit for DC bias of the graphene transistor, or for applying a bias to the NC bar. For AC measurements, the current signal was converted into voltage by a transimpedance amplifier (DL1211) with conversion factor $C = 10^{-4}\,\text{A}\,\text{V}^{-1}$, whose output signal was measured by a Signal Recovery 7265 lock-in amplifier. The AC photocurrent is given by $I_{AC} = V_{lockin}\pi C/\sqrt{2}$.

The precise determination of the phase of the AC signal can be affected by the mechanical chopper and the electronic equipment. Thus, we had calibrated the phase delay due to the setup with respect to the light signal using a fast Si Photodiode (Thorlabs DET10A2), which did not add any phase delay. This calibration was performed at each measurements run.

Supporting Information

Supporting Information is available from the Wiley Online Library or from the author.

Acknowledgements

Conflict of Interest

The authors declare no conflict of interest.

Data Availability Statement

The data that support the findings of this study are available from the corresponding author upon reasonable request.

Keywords

[1] M. Li, J.-S. Chen, M. Cotlet, *ACS Energy Lett.* **2019**, *4*, 2323.
[2] S. Padgaonkar, J. N. Olding, L. J. Lauhon, M. C. Hersam, E. A. Weiss, *Acc. Chem. Res.* **2020**, *53*, 763.
[3] X. Zhu, N. R. Monahan, Z. Gong, H. Zhu, K. W. Williams, C. A. Nelson, *J. Am. Chem. Soc.* **2015**, *137*, 8313.
[4] M. H. Kang, S. H. Kim, S. Jang, J. E. Lim, H. Chang, K. Kong, S. Myung, J. K. Park, *RSC Adv.* **2018**, *8*, 28447.
[5] R. Saran, R. J. Curry, *Nat. Photonics* **2016**, *10*, 81.
[6] G. Konstantatos, *Nat Commun* **2018**, *9*, 5266.
[7] G. Konstantatos, M. Badioli, L. Gaudreau, J. Osmond, M. Bernechea, F. P. G. de Arquer, F. Gatti, F. H. L. Koppens, *Nat Nano* **2012**, *7*, 363.
[8] D. Spirito, S. Kudera, V. Miseikis, C. Giansante, C. Coletti, R. Krahne, *J. Phys. Chem. C* **2015**, *119*, 23859.
[9] A. Ambrosi, C. K. Chua, A. Bonanni, M. Pumera, *Chem. Rev.* **2014**, *114*, 7150.
[10] F. Zhou, J. Chen, X. Tao, X. Wang, Y. Chai, *Research* **2019**, *2019*, 9490413.
[11] S. Bertolazzi, P. Bondavalli, S. Roche, T. San, S.-Y. Choi, L. Colombo, F. Bonaccorso, P. Samorì, *Adv. Mater.* **2019**, *31*, 1806663.
[12] X.-F. Wang, H. Tian, H.-M. Zhao, T.-Y. Zhang, W.-Q. Mao, Y.-C. Qiao, Y. Pang, Y.-X. Li, Y. Yang, T.-L. Ren, *Small* **2018**, *14*, 1702525.
[13] M. M. Rehman, H. M. M. U. Rehman, J. Z. Gul, W. Y. Kim, K. S. Karimov, N. Ahmed, *Sci. Technol. Adv. Mater.* **2020**, *21*, 147.
[14] S. Cui, S. Mao, G. Lu, J. Chen, *J. Phys. Chem. Lett.* **2013**, *4*, 2441.
[15] H. Hashtroudi, I. D. R. Mackinnon, M. Shafiei, *J. Mater. Chem. C* **2020**, *8*, 13108.
[16] A. De Iacovo, C. Venettacci, L. Colace, L. Scopa, S. Foglia, *IEEE Photonics Technol. Lett.* **2017**, *29*, 703.
[17] D. So, G. Konstantatos, *Chem. Mater.* **2015**, *27*, 8424.
[18] B. Martín-García, Y. Bi, M. Prato, D. Spirito, R. Krahne, G. Konstantatos, I. Moreels, *Sol. Energy Mater. Sol. Cells* **2018**, *183*, 1.
[19] F. Bonaccorso, Z. Sun, T. Hasan, A. C. Ferrari, *Nat. Photonics* **2010**, *4*, 611.
[20] G. Fiori, F. Bonaccorso, G. Iannaccone, T. Palacios, D. Neumaier, A. Seabaugh, S. K. Banerjee, L. Colombo, *Nat. Nanotechnol.* **2014**, *9*, 768.
[21] F. H. L. Koppens, T. Mueller, P. Avouris, A. C. Ferrari, M. S. Vitiello, M. Polini, *Nat. Nanotechnol.* **2014**, *9*, 780.
[22] A. De Sanctis, J. D. Mehew, M. F. Craciun, S. Russo, *Materials* **2018**, *11*, 1762.
[23] Y. Che, X. Cao, Y. Zhang, J. Yao, *J. Mater. Sci.* **2021**, *56*, 2341.
[24] I. Nikitskiy, S. Goossens, D. Kufer, T. Lasanta, G. Navickaite, F. H. L. Koppens, G. Konstantatos, *Nat. Commun.* **2016**, *7*, 11954.
[25] D. Kufer, T. Lasanta, M. Bernechea, F. H. L. Koppens, G. Konstantatos, *ACS Photonics* **2016**, *3*, 1324.
[26] Y. Yu, Y. Zhang, X. Song, H. Zhang, M. Cao, Y. Che, H. Dai, J. Yang, H. Zhang, J. Yao, *ACS Photonics* **2017**, *4*, 950.
[27] R. Waser, R. Dittmann, G. Staikov, K. Szot, *Adv. Mater.* **2009**, *21*, 2632.
[28] M. Lanza, H.-S. P. Wong, E. Pop, D. Ielmini, D. Strukov, B. C. Regan, L. Larcher, M. A. Villena, J. J. Yang, L. Goux, A. Belmonte, Y. Yang, F. M. Puglisi, J. Kang, B. Magyari-Köpe, E. Yalon, A. Kenyon, M. Buckwell, A. Mehonic, A. Shluger, H. Li, T.-H. Hou, B. Hudec, D. Akinwande, R. Ge, S. Ambrogio, J. B. Roldan, E. Miranda, J. Suñe, et al., *Adv. Electron. Mater.* **2019**, *5*, 1800143.
[29] Q. Zhao, Z. Xie, Y.-P. Peng, K. Wang, H. Wang, X. Li, H. Wang, J. Chen, H. Zhang, X. Yan, *Mater. Horiz.* **2020**, *7*, 1495.
[30] J. Zhu, T. Zhang, Y. Yang, R. Huang, *Appl. Phys. Rev.* **2020**, *7*, 011312.
[31] X. Zhu, D. Li, X. Liang, W. D. Lu, *Nat. Mater.* **2019**, *18*, 141.
[32] R. Waser, R. Dittmann, S. Menzel, T. Noll, *Faraday Discuss.* **2019**, *213*, 11.
[33] S. Casaluci, M. Gemmi, V. Pellegrini, A. D. Carlo, F. Bonaccorso, *Nanoscale* **2016**, *8*, 5368.
[34] A. Capasso, S. Bellani, A. L. Palma, L. Najafi, A. E. D. R. Castillo, N. Curreli, L. Cinà, V. Miseikis, C. Coletti, G. Calogero, V. Pellegrini, A. D. Carlo, F. Bonaccorso, *2D Mater.* **2019**, *6*, 035007.
[35] I. Riess, *Solid State Ionics* **2003**, *157*, 1.
[36] J. Peng, Y. Liu, Y. Pan, J. Wu, Y. Su, Y. Guo, X. Wu, C. Wu, Y. Xie, *J. Am. Chem. Soc.* **2020**, *142*, 18645.
[37] I. Valov, W. D. Lu, *Nanoscale* **2016**, *8*, 13828.
[38] A. Agresti, S. Pescetelli, A. L. Palma, B. Martín-García, L. Najafi, S. Bellani, I. Moreels, M. Prato, F. Bonaccorso, A. Di Carlo, *ACS Energy Lett.* **2019**, *4*, 1862.

ADVANCED SCIENCE NEWS
www.advancedsciencenews.com

PSSrrl
physica status solidi
www.pss-rapid.com

[39] M. Kazes, S. Buhbut, S. Itzhakov, O. Lahad, A. Zaban, D. Oron, *J. Phys. Chem. Lett.* **2014**, *5*, 2717.

[40] K. J. Tielrooij, L. Orona, A. Ferrier, M. Badioli, G. Navickaite, S. Coop, S. Nanot, B. Kalinic, T. Cesca, L. Gaudreau, Q. Ma, A. Centeno, A. Pesquera, A. Zurutuza, H. de Riedmatten, P. Goldner, F. J. García de Abajo, P. Jarillo-Herrero, F. H. L. Koppens, *Nat. Phys.* **2015**, *11*, 281.

[41] L. Gaudreau, K. J. Tielrooij, G. E. D. K. Prawiroatmodjo, J. Osmond, F. J. G. de Abajo, F. H. L. Koppens, *Nano Lett.* **2013**, *13*, 2030.

[42] A. Boulesbaa, K. Wang, M. Mahjouri-Samani, M. Tian, A. A. Puretzky, I. Ivanov, C. M. Rouleau, K. Xiao, B. G. Sumpter, D. B. Geohegan, *J. Am. Chem. Soc.* **2016**, *138*, 14713.

[43] M. Li, J.-S. Chen, P. K. Routh, P. Zahl, C.-Y. Nam, M. Cotlet, *Adv. Funct. Mater.* **2018**, *28*, 1707558.

[44] X. Feng, Z. He, W. Zhu, M. Zhao, Z. Liu, S. Yang, S. Tang, Q. Guo, Z. Jin, D. Chen, G. Ding, G. Wang, *J. Mater. Chem. C* **2021**, *9*, 609.

[45] D. Bozyigit, W. M. M. Lin, N. Yazdani, O. Yarema, V. Wood, *Nat. Commun.* **2015**, *6*, 6180.

[46] H. Roshan, F. Ravanan, M. H. Sheikhi, A. Mirzaei, *J. Alloys Compd.* **2021**, *852*, 156948.

[47] B. Martín-García, D. Spirito, R. Krahne, I. Moreels, *J. Mater. Chem. C* **2018**, *6*, 13128.

[48] K. Terabe, T. Hasegawa, T. Nakayama, M. Aono, *Nature* **2005**, *433*, 47.

[49] Z. Xu, Y. Bando, W. Wang, X. Bai, D. Golberg, *ACS Nano* **2010**, *4*, 2515.

[50] C. Lutz, T. Hasegawa, T. Chikyow, *Nanoscale* **2016**, *8*, 14031.

[51] S. Kim, J. Nah, I. Jo, D. Shahrjerdi, L. Colombo, Z. Yao, E. Tutuc, S. K. Banerjee, *Appl. Phys. Lett.* **2009**, *94*, 062107.

[52] S. M. Song, B. J. Cho, *Nanotechnology* **2010**, *21*, 335706.

[53] J. Sforzini, P. Hapala, M. Franke, G. van Straaten, A. Stöhr, S. Link, S. Soubatch, P. Jelínek, T.-L. Lee, U. Starke, M. Švec, F. C. Bocquet, F. S. Tautz, *Phys. Rev. Lett.* **2016**, *116*, 126805.

[54] S. A. E. Al-Bluwi, A. Al-Ghamdi, G. Baell, *Optik* **2020**, *205*, 164264.

[55] J. Halme, *Phys. Chem. Chem. Phys.* **2011**, *13*, 12435.

[56] N. Curreli, M. Serri, D. Spirito, E. Lago, E. Petroni, B. Martín-García, A. Politano, B. Gürbulak, S. Duman, R. Krahne, V. Pellegrini, F. Bonaccorso, *Adv. Funct. Mater.* **2020**, *30*, 1908427.

[57] A. Robin, E. Lhuillier, X. Z. Xu, S. Ithurria, H. Aubin, A. Ouerghi, B. Dubertret, *Sci. Rep.* **2016**, *6*, 24909.

[58] S. H. Liu, *Phys. Rev. Lett.* **1985**, *55*, 529.

[59] J. Bisquert, A. Compte, *J. Electroanal. Chem.* **2001**, *499*, 112.

[60] J. Tang, R. A. Marcus, *Phys. Rev. Lett.* **2005**, *95*, 107401.

[61] L. A. Dissado, R. M. Hill, *Phys. Rev. B* **1988**, *37*, 3434.

[62] A. Le Mehaute, *J Stat Phys* **1984**, *36*, 665.

[63] D. Prasai, A. R. Klots, A. Newaz, J. S. Niezgoda, N. J. Orfield, C. A. Escobar, A. Wynn, A. Efimov, G. K. Jennings, S. J. Rosenthal, K. I. Bolotin, *Nano Lett.* **2015**, *15*, 4374.

[64] H. Yin, A. Akey, R. Jaramillo, *Phys. Rev. Materials* **2018**, *2*, 084602.

[65] C. Spindler, T. Galvani, L. Wirtz, G. Rey, S. Siebentritt, *J. Appl. Phys.* **2019**, *126*, 175703.

[66] Z. Sun, Z. Liu, J. Li, G. Tai, S.-P. Lau, F. Yan, *Adv. Mater.* **2012**, *24*, 5878.

[67] S. Ghosh, A. Winchester, B. Muchharla, M. Wasala, S. Feng, A. L. Elias, M. B. M. Krishna, T. Harada, C. Chin, K. Dani, S. Kar, M. Terrones, S. Talapatra, *Sci. Rep.* **2015**, *5*, 11272.

[68] P. Yu, Q. Zeng, C. Zhu, L. Zhou, W. Zhao, J. Tong, Z. Liu, G. Yang, *Adv. Mater.* **2021**, *33*, 2005607.

[69] D. Paria, H.-H. Jeong, V. Vadakkumbatt, P. Deshpande, P. Fischer, A. Ghosh, A. Ghosh, *Nanoscale* **2018**, *10*, 7685.

[70] S. V. Rempel, Yu. V. Kuznetsova, E. Yu. Gerasimov, A. A. Rempel, *Phys. Solid State* **2017**, *59*, 1629.

[71] X. Wu, P. L. Redmond, H. Liu, Y. Chen, M. Steigerwald, L. Brus, *J. Am. Chem. Soc.* **2008**, *130*, 9500.

[72] Y. Zhang, X. Yang, P. Wei, P. X. Liu, *IET Control Theory Appl.* **2020**, *14*, 2556.

[73] V. Miseikis, D. Convertino, N. Mishra, M. Gemmi, T. Mashoff, S. Heun, N. Haghighian, F. Bisio, M. Canepa, V. Piazza, C. Coletti, *2D Mater.* **2015**, *2*, 014006.

[74] V. Miseikis, F. Bianco, J. David, M. Gemmi, V. Pellegrini, M. Romagnoli, C. Coletti, *2D Mater.* **2017**, *4*, 021004.

[75] M. A. Giambra, V. Mišeikis, S. Pezzini, S. Marconi, A. Montanaro, F. Fabbri, V. Sorianello, A. C. Ferrari, C. Coletti, M. Romagnoli, *ACS Nano* **2021**, *15*, 3171.

[76] Q. A. Akkerman, B. Martín-García, J. Buha, G. Almeida, S. Toso, S. Marras, F. Bonaccorso, U. Petralanda, I. Infante, L. Manna, *Chem. Mater.* **2019**, *31*, 8145.

[77] S. Toso, Q. A. Akkerman, B. Martín-García, M. Prato, J. Zito, I. Infante, Z. Dang, A. Moliterni, C. Giannini, E. Bladt, I. P. Lobato Hoyos, J. Ramade, S. Bals, J. Buha, D. Spirito, E. Mugnaioli, M. Gemmi, L. Manna, *J. Am. Chem. Soc.* **2020**, *142*, 10198.